Multiscale Pseudoatomistic Quantum Transport Modeling for van der Waals Heterostructures

Giuseppe Lovarelli,[1,2,*] Gaetano Calogero,[1,3] Gianluca Fiori,[1] and Giuseppe Iannaccone[1]

[1] *Dipartimento di Ingegneria dell'Informazione, Università di Pisa, Pisa 56122, Italy*
[2] *Dipartimento di Fisica E. Fermi, Università di Pisa, Pisa 56127, Italy*
[3] *Consiglio Nazionale delle Ricerche CNR-IMM, Z.I. VIII Strada 5, Catania 95121, Italy*

(Received 10 November 2021; revised 19 April 2022; accepted 13 June 2022; published 19 September 2022)

Several electronic and optoelectronic devices have been proposed in recent years based on vertical heterostructures of two-dimensional (2D) materials. The large number of combinations of available 2D materials and the even larger number of possible heterostructures require effective and predictive device-simulation methods, to inform and accelerate experimental research and to support the interpretation of experiments. Here, we propose a computationally effective and physically sound method to model electron transport in 2D van der Waals heterostructures, based on a multiscale approach and quasiatomistic Hamiltonians. The method uses *ab initio* simulations to extract the parameters of a simplified tight-binding Hamiltonian based on a uniform three-dimensional lattice geometry that enables device simulations using the nonequilibrium Green's function approach in a computationally effective way. We describe the application and limitations of the method and discuss the examples of two use cases of practical electronic devices based on 2D materials, such as a field-effect transistor and a floating-gate memory, composed of molybdenum disulphide, hexagonal boron nitride and graphene.

DOI: 10.1103/PhysRevApplied.18.034045

I. INTRODUCTION

Vertical heterostructures (VHs) of two-dimensional (2D) materials are an ingenious means of implementing the "materials-on-demand" paradigm for nanoelectronics [1–4], which can enable the design of materials optimized for specific applications at an atom-by-atom level. The rapid progress in growth and fabrication techniques [5–9] is indeed offering unprecedented opportunities for tailoring such one-atom-thick building blocks into band-engineered platforms for memory devices [10], field-effect transistors (FETs) [3,11], flexible electronics [12], and optoelectronics [13,14].

From the point of view of devising a device concept, we would like to estimate—possibly using device simulations before actual sample fabrication—the properties of quantum transport in the "vertical" direction, i.e., the direction perpendicular to the 2D material planes. There are a few devices in which this aspect is extremely important: for example, in solar cells and in optoelectronic devices, performance is strictly dependent on the vertical-transport properties [13–15]; in FETs, vertical transport through the gate stack is an important factor of static power consumption [16,17]; in a floating-gate nonvolatile memory, vertical quantum transport determines the time required to program and erase the memory, and its retention property [18,19]. In addition, by choosing and engineering the sequence of 2D layers in the vertical heterostructure, we can tune the vertical-transport properties and therefore the device operation.

Ensuring rapid and cost-effective progress toward fabrication and prototyping requires materials and device design based on predictive simulations. However, the modeling and understanding of vertical transport through stacked 2D materials presents several challenges [20]. From an electronic structure point of view, every 2D material is characterized by its own specific lattice geometry and symmetry, which define a specific Brillouin zone that often does not match with that of other components in a heterostructure: the weak van der Waals interlayer interactions allow stacked 2D materials to have different lattice structures without introducing strain.

The final properties of the heterostructure often depend on the relative alignment between adjacent layers, which determines the interlayer coupling strength. This effect can be very drastic, as observed in the induced superconductivity in bilayer graphene at certain "magic" angles

* giuseppe.lovarelli@gmail.com

[21]. Relative alignment is not only hard to control during fabrication but also represents a major challenge from a modeling perspective. Very large—and computationally hard to treat—periodic unit cells are needed to describe the whole heterostructure to reproduce the band structure of the individual components and the local electronic features at the interfaces. In practice, only vertical stacks with basic alignment and good lattice matching are modeled with atomistic detail, using *ab initio* methods such as density functional theory (DFT), and are therefore limited to a few selected configurations. Good progress in this direction has been made since the introduction of density-functional tight-binding (DFTB) methods [22–24]; here, however, we prefer to consider a more manageable approach and postpone the application of DFTB models to future works.

In addition, when the electron-transport problem under far-from-equilibrium bias has to be taken into account, a significant complexity is added to the calculation of the vertical current, where one usually combines the nonequilibrium Green's function (NEGF) formalism with Poisson's equation [25,26]. Given the large bias voltage applied in the device examples mentioned above, that becomes very challenging if done from first principles.

Researchers have often made strong approximations to reduce the complexity of simulations, such as assuming translation symmetry of the Hamiltonian in the transversal direction and therefore separating the Schrödinger equation into a one-dimensional (1D) equation in the vertical direction, enabling the calculation of transmission probabilities, and a 2D equation in the transversal equation, providing information on the density of states. This approximation leads to the Esaki-Tsu current formula [27], which can capture most of the relevant transport physics in the case of III-V heterostructures, where the materials of adjacent layers are quite similar [28–30] (sometimes leaving out important effects [31]), but is unreasonable in the case of vertical heterostructures of 2D materials, where stacked layers can have very different band structures. In more recent years, some analytical models have been developed with the idea of studying vertical transport across stacks of monolayers [32,33]. However, these models are limited by the choice of the eigenfunctions of the source and drain materials, as they need to be described by the same basis set. In particular, this requires that the source and drain are made of the same material. In this paper, we propose a multiscale pseudoatomistic method that overcomes this limitation and therefore applies to a more general class of vertical heterostructures of 2D materials. This model enables us to capture the relevant electronic structure and its effect on vertical transport in a much better way than the unrealistic assumption of translation symmetry in the transversal direction, and it is much more tractable than a full *ab initio* or atomistic simulation of the full heterostructure from a computational point of view. In the method that we propose, *ab initio* DFT simulations are used to extract the parameters of a pseudoatomistic Hamiltonian of the whole heterostructure, which is then used to solve the transport problem and the electrostatics in a self-consistent way.

To describe two practical uses of the method, we show its application to the simulation of a FET and a floating-gate memory, with both devices based on a vertical heterostructure of van der Waals materials: molybdenum disulphide (MoS_2) as the channel, hexagonal boron nitride (*h*-BN) as the insulator, and graphene (Gr) as the floating gate. We focus in both cases on the simulation of the tunneling current through the dielectric, for the calculation of the gate leakage in the case of the FET and of the retention time of the memory, which requires the time-dependent self-consistent solution of the transport and electrostatics problems.

II. PSEUDOATOMISTIC HAMILTONIAN OF A VERTICAL HETEROSTRUCTURE BASED ON *ab initio* SIMULATIONS

Here, we propose an effective approach to study electron transport across vertical heterostructures based on tight binding. In particular, as the van der Waals cross-plane interactions are weak, we expect this effective model not to deviate too strongly from the tight-binding model of the single isolated monolayers. Instead of considering a supercell, which is very expensive from a computational point of view, we construct a vertical pseudocrystal in which each layer presents the same translational invariance and the same fundamental cell size. We accept that this common-lattice approximation introduces some inaccuracies and are satisfied as long as we are able to reproduce the profile of the cross-plane transmission spectrum $T(E)$ obtained by means of DFT. For simplicity, we consider a ballistic approximation for our model, so that the vertical momentum of the charges is conserved; but we expect also inelastic relaxation phenomena to take place, as they could connect states at different wave vectors. Therefore, for each component material M, we consider the monolayer DFT-computed local density of states $\mathrm{LDOS}(E;M)$ and replicate it by means of the tight-binding model. Next, we fix the band alignment and the cross-plane coupling parameters and we do so by considering some small selected heterostructures and their LDOS and transmission spectra. At the DFT level, because the supercell required to model a simple heterostructure can be extremely large, we can consider only a limited number of structures. By means of our effective model, we can assemble them and study a complete electron device.

A. Modeling the monolayers

Each isolated layer in the heterostructure is assumed to be infinite in the x-y plane and is described by a two-center Hamiltonian P. By making use of Bloch's theorem, P can

be written as

$$P(\mathbf{k}) = \begin{pmatrix} \varepsilon_A + t_A f_2(\mathbf{k}) & t f_1(\mathbf{k}) \\ t^* f_1{}^*(\mathbf{k}) & \varepsilon_B + t_B f_2(\mathbf{k}) \end{pmatrix}, \tag{1}$$

where the ε_i $(i = A, B)$ represent the on-site energies, t is the nearest-neighbor hopping parameter, t_i are the second-nearest-neighbor hopping parameters, and $f_1(\mathbf{k})$ and $f_2(\mathbf{k})$ are functions of the in-plane momentum $\mathbf{k} = (k_x, k_y)$, which depend on the geometry of the system and refer to first- and second-nearest-neighboring atoms, respectively [34]. For a hexagonal lattice, such as the one shown in Fig. 1(a), these functions can be written as

$$\begin{cases} f_1(\mathbf{k}) = 1 + 2e^{-ik_x \frac{\sqrt{3}}{2} a} \cos\left(k_y \dfrac{a}{2}\right) \\ f_2(\mathbf{k}) = 4 \cos\left(k_y \dfrac{a}{2}\right) \cos\left(k_x \dfrac{\sqrt{3}}{2} a\right) + \\ \qquad\qquad + 2 \cos\left(k_y a\right) = |f_1(\mathbf{k})|^2 - 3, \end{cases} \tag{2}$$

where a is the lattice constant. With this model, we can describe a direct band gap the width of which is expressed as $E_g = (\varepsilon_A + 3t_A) - (\varepsilon_B + 3t_B)$; it is easy to see that when no second-nearest-neighbor interaction is considered, this relation reduces to the usual $E_g = \varepsilon_A - \varepsilon_B$ [35]. The on-site energies $\varepsilon_{A,B}$ can be arbitrarily shifted by a quantity E_0, as long as $\Delta = \varepsilon_A - \varepsilon_B$ does not change. This freedom allows us to carry out band alignment in the heterostructure by simply changing E_0. In the present work, these shifts are found by analyzing the *ab initio* layer-resolved LDOS (see Sec. III).

B. Modeling the off-plane couplings

Since no periodicity can be imposed along the vertical axis z, the Hamiltonian for the full system needs to be written in real space. As we are working in the common-lattice approximation, we recall that the lattices for each monolayer are perfectly aligned one on top of another. Therefore, for a stack of L layers, the Hamiltonian takes the block-tridiagonal form

$$H(\mathbf{k}) = \begin{pmatrix} P_1(\mathbf{k}) & V_{1,2}(\mathbf{k}) & & & \\ V_{1,2}^\dagger(\mathbf{k}) & P_2(\mathbf{k}) & V_{2,3}(\mathbf{k}) & & \\ & \ddots & \ddots & \ddots & \\ & & V_{L-2,L-1}^\dagger(\mathbf{k}) & P_{L-1}(\mathbf{k}) & V_{L-1,L}(\mathbf{k}) \\ & & & V_{L-1,L}^\dagger(\mathbf{k}) & P_L(\mathbf{k}) \end{pmatrix}, \tag{3}$$

where for $l = 1, \ldots, L$, $V_{l,l+1}(\mathbf{k})$ is the interlayer-hopping matrix between layers l and $l+1$, with $V_{l,l+1}^\dagger = V_{l+1,l}$ being its conjugate transpose; $P_l(\mathbf{k})$ is the in-plane Hamiltonian in the form of Eq. (1) and the empty spaces are 0.

If two adjacent layers correspond to the same material, we write $V_{l,l+1}(\mathbf{k})$ as

$$V_{l,l+1}(\mathbf{k}) = \begin{pmatrix} v_A & v f_1(\mathbf{k}) \\ v^* f_1{}^*(\mathbf{k}) & v_B \end{pmatrix}, \tag{4}$$

where v is the off-plane hopping parameter between nearest-neighbor atoms and v_i $(i = A, B)$ corresponds to the next-nearest-neighbor ones [see Fig. 1(b)]; otherwise, if the two layers are of different materials,

$$V_{l,l+1}(\mathbf{k}) = \begin{pmatrix} v_0 & v_1 f_1(\mathbf{k}) \\ v_1^* f_1{}^*(\mathbf{k}) & v_0 \end{pmatrix}, \tag{5}$$

where v_0 is the interface off-plane hopping parameter for the nearest atom and v_1 is the corresponding parameter for the next-nearest ones [see Fig. 1(c)].

III. PARAMETRIZATION OF A MoS_2/*h*-BN/Gr HETEROSTRUCTURE

As an example for the presented model, we consider a VH composed of a monolayer of MoS_2, a multilayer of *h*-BN, and a monolayer of graphene (Gr); these materials are the building blocks of several electronic devices based on van der Waals heterostructures reported in the literature [10,36–41]. The reason why these materials are very often used is simple: *h*-BN is the best-performing 2D insulator, MoS_2 is probably the most promising 2D semiconductor in terms of its energy gap and in-plane mobility, and graphene is a 2D semimetal, with the highest mobility and conductivity. Their combination in van der Waals heterostructures enables us to obtain different functional materials.

In order to choose the parameters for the Hamiltonian given in Eq. (3) for such a structure, we follow the procedure illustrated in Fig. 2 and already explained at the beginning of Sec. II. The electronic band structure for a monolayer of each material is obtained in a quite straightforward manner, as we extract the parameters appearing in

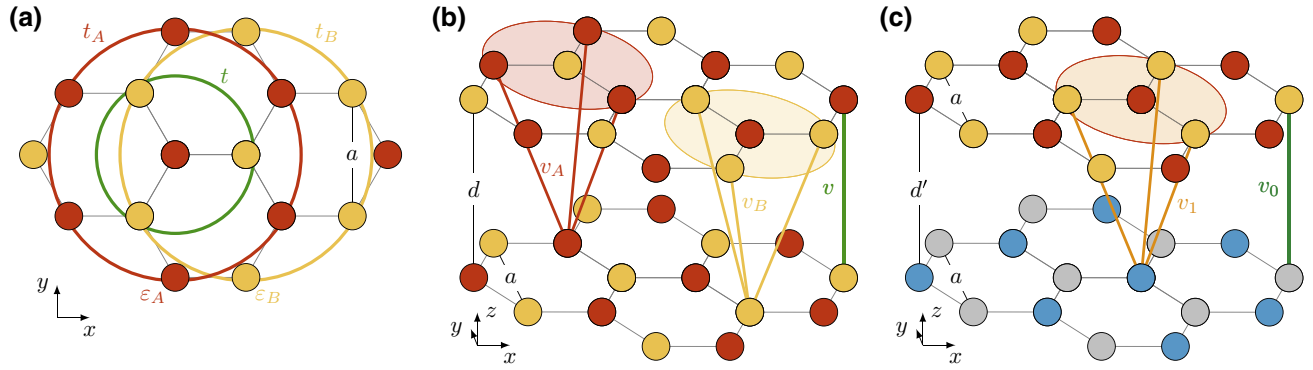

FIG. 1. (a) A planar representation of the hexagonal lattice with the two centers A (red) and B (yellow), along with the first-nearest-neighbor and second-nearest-neighbor in-plane hopping parameters. (b) A schematic representation of the pseudolattice describing two AA' stacked layers of the same material, with off-plane nearest-neighbor (next-nearest-neighbor) hopping indicated by dark (light) green lines. (c) The pseudolattice for two AA' stacked layers of different materials, with off-plane nearest-neighbor (next-nearest-neighbor) hopping indicated by dark (light) blue lines.

Eq. (1) by matching the energy gap and band curvature for every DFT-simulated monolayer. Note that as long as a single monolayer is considered, the lattice constant does not influence any of the electronic properties, because we sum over all the infinite number of in-plane momenta $\mathbf{k}$. We choose the lattice parameter of MoS_2 as a reference for the common lattice, as it is the largest, and set $a_{VH} = a_{MoS_2}$. To see the comparison between the DFT bands, also shown in Fig. 3, and those obtained from tight binding on the common lattice, all centered around the K point of the respective material, refer to Appendix A. The band alignment follows by considering the LDOS for two different heterostructures: one composed of Gr and h-BN and the other of h-BN and MoS_2. As h-BN is present in both of them, we use it as a reference. If Δ_1 is the valence-band offset between Gr and h-BN (the energy of the top of the valence band for Gr is taken to be its work function) and Δ_2 is the valence-band offset between MoS_2 and h-BN, then $\Delta_1 - \Delta_2$ is taken as the valence-band offset between Gr and MoS_2.

Lastly, we obtain the off-plane hopping parameters appearing in Eqs. (4) and (5) by scanning the phase space and selecting the ones that best reproduce the cross-plane transmission. Apart from the two aforementioned structures that give the intermaterial hopping parameters, we also consider bulk stacked h-BN, as it is our tunneling material.

The modeling of contacts is a delicate matter; for simplicity, we consider a 1D system. Therefore, we construct the MoS_2 and Gr contacts by adding layers for each of them. The Gr layers are coupled by selecting the off-plane parameters that best reproduce the DFT transmission for bulk graphite; the MoS_2 ones are instead coupled in such a way that its band gap is not altered very much. The resulting hopping parameters are reported in Table I.

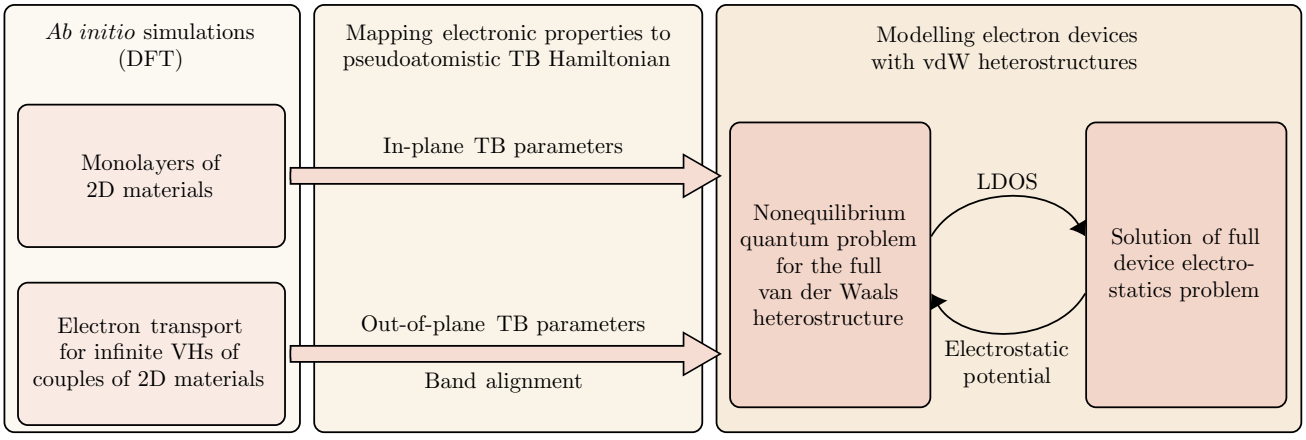

FIG. 2. The scheme of the multiscale simulation procedure. *Ab initio* (DFT) simulations are used to extract the parameters of the tight-binding Hamiltonian, which is then used in the self-consistent simulation of quantum transport and electrostatics.

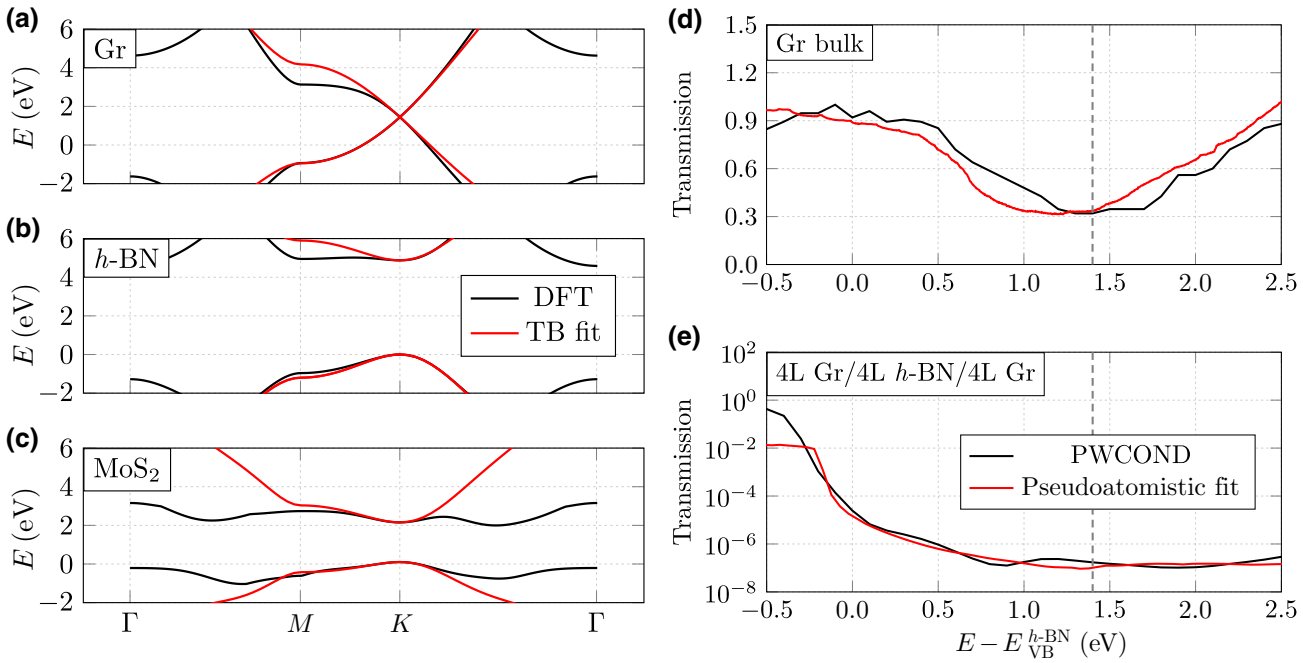

FIG. 3. A comparison of the band structures for various materials, as computed by DFT and by the effective model on the real lattice. The band structure on the common lattice for Gr and *h*-BN is reported in Appendix A. (a)–(c) Tight binding versus DFT on the real lattice band structures. After the fit, the *h*-BN band gap is artificially widened to match that in the transmission spectrum; for further details, see Appendix C. (d) Vertical transmission for bulk Gr (12 layers, linear scale) and (e) for *h*-BN embedded in Gr (4L, four layers; 12 layers in total, logarithmic scale). The dashed line indicates the Dirac-cone energy for graphene.

A. DFT simulations

All our calculations are performed with the QUANTUM ESPRESSO electronic structure package [47,48], using ultrasoft pseudopotentials, the generalized gradient approximation–Perdew-Burke-Ernzerhof (GGA-PBE) exchange-correlation functional [49] with D2 van der Waals correction [50], an energy cutoff of 40 Ry, and a charge-density cutoff of 400 Ry. The Brillouin zone of all monolayer materials is sampled with a $15 \times 15 \times 1$ Monkhorst-Pack grid (increased to $30 \times 30 \times 1$ for computing DOS). For bulk materials, six k points are used to sample the out-of-plane direction (increased to 12 for DOS). The equilibrium in-plane lattice parameter a and interlayer distance d for Gr are obtained by relaxing all atomic coordinates self-consistently until all residual forces acting on each atom are below 10^{-3} Ry/Bohr. We find $a = 0.246$ nm and $d = 0.333$ nm, in good agreement with the experimental values [51]. The *h*-BN in-plane lattice parameter is adapted to that of Gr, with a compression of less than 2% compared to its equilibrium geometry. In the case of the *h*-BN/MoS_2 VHs, to compensate for the large mismatch between MoS_2 and the compressed

TABLE I. The in-plane parameters for monolayer *h*-BN, Gr, and MoS_2 and the off-plane parameters for the tight-binding model. The table is organized into two parts: in the first, we show the in-plane parameters obtained by fitting the band structure of each material as computed by DFT (the DFT lattice); in the second, we show the ones found for the common lattice (for the vertical heterostructure, we choose $a_{VH} = a_{MoS_2}$). The interplane parameters are fitted from the transmission spectra in Fig. 3. The intermaterial hopping parameters v_0 and v_1 refer to the coupling with *h*-BN. Distances are expressed in nanometers and everything else in electronvolts.

	a (nm)	E_g	Δ	t	t_A	t_B	d (nm)	v	v_A	v_B	$v_0^{h\text{-BN}}$	$v_1^{h\text{-BN}}$
DFT lattice												
h-BN	0.246	4.86	5.77	−2.28	−0.22	0.07	0.333					
Gr	0.246	0	0	−2.50	0.17	0.17	0.333					
MoS_2	0.307	2.05	0.58	−1.81	−0.07	0.42	0.615					
Common lattice												
h-BN	0.307	4.86	5.42	−1.90	−0.13	0.05	0.333	0.25	0.25	0		
Gr	0.307	0	0	−1.98	−0.09	−0.09	0.333	1.45	0.80	0.80	-6.00	5.00
MoS_2	0.307	2.05	0.58	−1.81	−0.07	0.42	0.615	0.17	0.15	0	0.15	0.25

h-BN, a supercell is constructed by attaching a MoS_2 4×4 supercell (48 atoms per layer) on a *h*-BN 5×5 supercell (50 atoms per layer). With this arrangement, we are able to ensure a tensile compression $< 3\%$ for MoS_2, the compressed lattice parameter of which is found to be $a = 0.307$ nm. The vertical interlayer distances within and between the materials are again optimized until the forces between the atoms are below 10^{-3} Ry/Bohr. In Table I, we report the lattice parameters and the in-plane hopping parameters as fitted from the monolayer DFT energy bands; graphical comparisons between the *ab initio* and the corresponding tight-binding band structures can be found in Figs. 3(a)–3(c). These are obtained by considering $a = 0.246$ nm for graphene and *h*-BN and $a = 0.307$ nm for MoS_2 and result in a band gap of 4.87 eV for *h*-BN and 2.05 eV for MoS_2, which is in good agreement with the literature [52,53]. From these values, we can extract the tight-binding parameters for monolayers of each individual material.

The *ab initio* transmission calculations are computed using the PWCOND postprocessing tool included in QUANTUM ESPRESSO [54], while sampling the periodic directions with a 30×30 *k*-point grid (91 within the irreducible Brillouin zone). The *h*-BN and Gr electrodes are simulated using their respective bulk unit cells (two layers); their homogeneous bulk-scattering regions are modeled using 12 layers in total. The Gr/*h*-BN VH is modeled by using four layers of *h*-BN embedded in four layers of graphene on either side, as illustrated in Fig. 4(a). The MoS_2/*h*-BN VH is instead modeled by using a monolayer of MoS_2 embedded in two layers of *h*-BN on each side, as illustrated in Fig. 4(b). The large number of atoms contained in the latter supercell (they are already 248 in the system considered here) is too large for the inclusion of more layers. The off-plane parameters appearing in Eqs. (4) and (5), and also reported in Table I, are obtained by fitting the transmission spectrum computed with PWCOND by using the NanoTCAD ViDES toolkit [55]. As an example, the results for the bulk graphite and Gr/*h*-BN/Gr heterostructures are reported in Figs. 3(d) and 3(e).

Band alignment is carried out by considering the relative valence-band offset among the three materials combined in the two aforementioned VHs; as *h*-BN is present in both of them, its valence-band top energy is taken as a reference. These offsets are extracted from the *ab initio* computed LDOS shown in Fig. 4(c) after proper alignment and are reported in Table II. We note that these values are quite different from those obtained from Anderson's rule using the electron affinity for the isolated materials available in the literature (also reported in Table II). Better agreement may be obtained by means of different DFT functionals, such as the Heyd-Scuseria-Ernzerhof hybrid functional (HSE06), or the GW approximation [56–59]; however, for consistency reasons, we will only consider the offsets computed in the present work. A comparison between the LDOS as computed both in DFT and by our tight-binding model is reported in Appendix B. Finally, the cross-plane energy gap for the stacked configurations is compared to the monolayer energy gap in Table III.

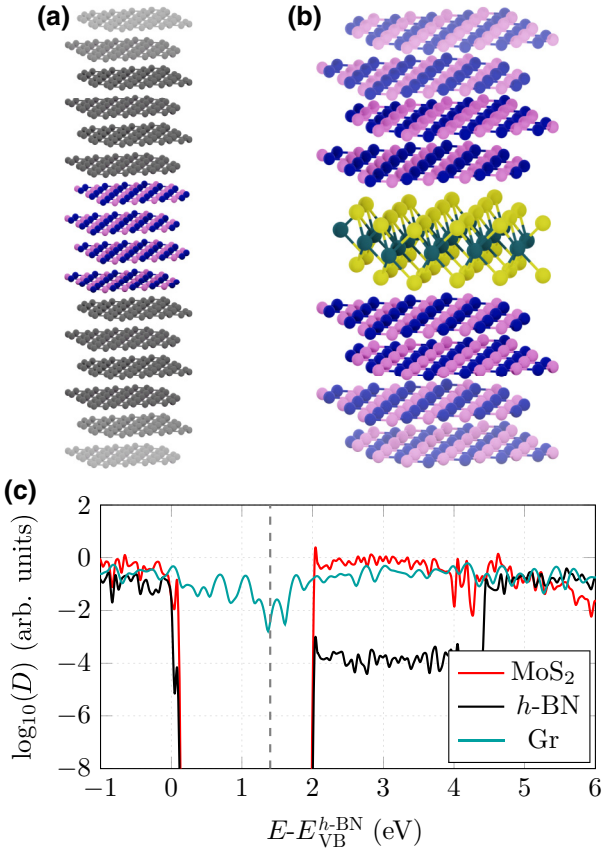

FIG. 4. Three-dimensional (3D) representations of the (a) Gr/*h*-BN/Gr and (b) *h*-BN/MoS_2/*h*-BN heterostructures used for band alignment. The semitransparent planes represent the electrodes, while the central part is the scattering region. (c) The density of states *D* for each material, after band alignment, as referred to the *h*-BN valence-band top. The dashed line indicates the Dirac-cone energy for graphene.

TABLE II. The valence-band energy offset with respect to *h*-BN, in electronvolts. In the first row, we report the valence-band offset (VBO) as found in the literature by following Anderson's rule, with the *h*-BN valence-band energy as found in Ref. [46]; in the second, we report the value obtained from the analysis of our *ab initio* DOS alignment.

Valence-band offset (eV)	MoS_2	Gr
Anderson's rule	0.6 [42–44]	2.1 [45]
This work	0.1	1.4

TABLE III. The band-gap comparison between the monolayer and stacked configurations for the three materials under consideration. The *h*-BN stacked gap refers to the bulk case, whereas the MoS_2 and Gr cases refer to the 2L-1L-2L *h*-BN/MoS_2/*h*-BN and 4L-4L-4L Gr/*h*-BN/Gr configurations, respectively.

	Monolayer (eV)	Stacked (eV)
h-BN	4.89	5.90
Gr	0	0
MoS_2	2.05	1.89

IV. USE OF PSEUDOLATTICE HAMILTONIANS IN DEVICE SIMULATION

As a demonstration use case, we show that the proposed methodology is very useful for simulating the gate-leakage current in a FET and the retention time of a floating-gate memory based on vertical heterostructures of 2D materials. In both cases, we consider the same core heterostructure, where a multilayer *h*-BN tunneling barrier separates a monolayer MoS_2 channel from a monolayer Gr gate and everything is placed above a SiO_2 substrate. This structure can represent the central region in a device such as those shown in Figs. 5(a) and 6(a). We assume that both devices are sufficiently well behaved from the electrostatics point of view, i.e., that the lateral device contacts have no influence on the region we are considering.

A. Leakage current in a FET

As introduced in Sec. II, we consider the bidimensional layers in the *x*-*y* plane to be infinite. This is a valid approximation if we are interested in the flat-potential region in the center of a FET with good electrostatics and it allows us to reduce the electrostatic problem to a 1D nonlinear Poisson's equation:

$$\vec{\nabla}\cdot\left[\epsilon_r(z)\vec{\nabla}\varphi(z)\right] = -\sum_m Q(z_m)\frac{\delta(z-z_m)}{\epsilon_0}, \qquad (6)$$

where φ and ϵ_r are the electrostatic potential and the relative dielectric constant along the z direction, respectively, $Q(z_m)$ is the charge per unit area on the mth layer, and ϵ_0 is the vacuum dielectric constant. The transport mechanism is studied in the NEGF framework [25]. Here, we need to describe two leads and we do so by adding some layers along the z direction: four Gr layers above the gate and four MoS_2 layers below the channel, as required by our solver, NanoTCAD ViDES [55]. We use the values reported in Table I for the off-plane coupling parameters, in order to leave the channel band-gap width unaltered. We also considered an n doping for the MoS_2 channel equal to $n = 5\times10^{12}$ cm^{-2} and a width-dependent dielectric constant for the *h*-BN barrier, with the values taken from Ref. [60].

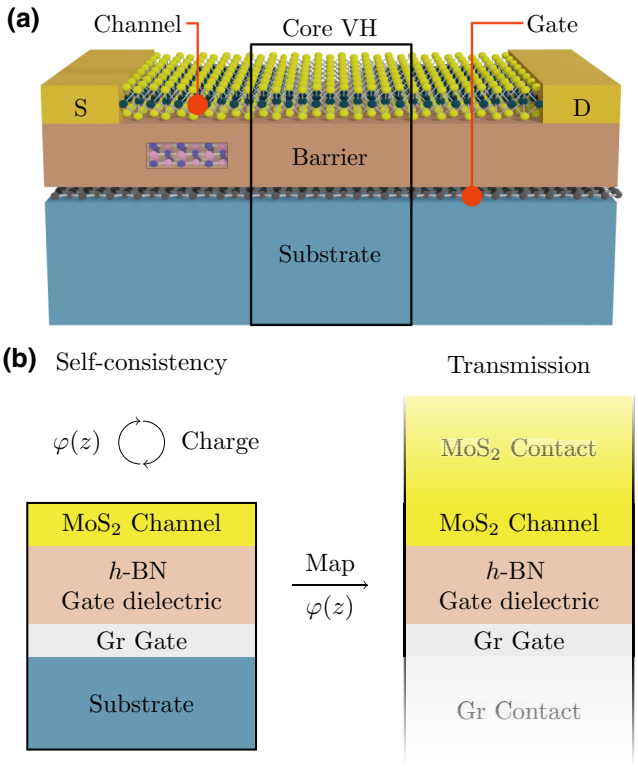

FIG. 5. (a) A view of the FET, with the core vertical heterostructure (and the substrate) highlighted. (b) The self-consistent scheme: the Fermi level of the semimetallic gate is used to self-consistently determine the potential everywhere along the device. The current is then obtained from the Büttiker-Landauer formula, after solving the NEGF problem.

The simulations are performed by following the procedure shown in Fig. 5(b) and outlined below. We consider the core heterostructure and apply an electrochemical potential μ_g on the gate and μ_c on the channel, resulting in an applied voltage between the gate and the channel of $V_{gc} = -e(\mu_g - \mu_c)$. The electrostatics equation is solved by means of Eq. (6), with Neumann boundary conditions imposed at the channel and at the gate; then the resulting electrostatic potential $\varphi(z)$ is used to compute the induced charge $Q(z_i)$ in these two regions:

$$Q[z_i;\varphi(z_i)] = -e\int D_i[E-\varphi(z_i)]f(E-\mu_i)\mathrm{d}E, \qquad (7)$$

where e is the elementary charge and D_i is the density of states of at the coordinate z_i. This procedure is repeated in a self-consistent Schrödinger-Poisson fashion to determine a good approximation of the electrostatic configuration of the device. NEGF is then applied to determine the total transmission spectrum $T(E)$ for the device. Finally, the Büttiker-Landauer formula is applied to find the leakage

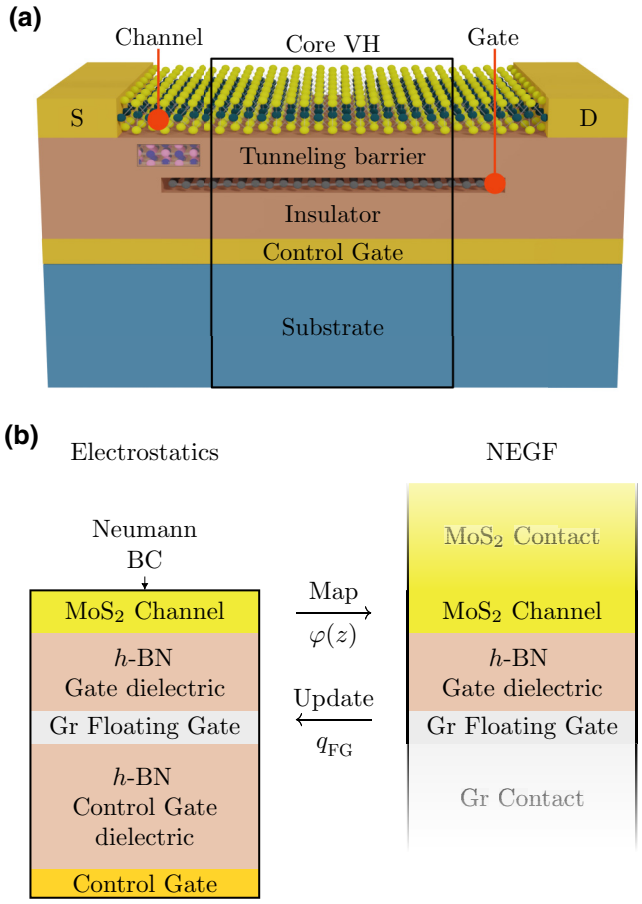

FIG. 6. (a) A view of the floating-gate memory, with the core vertical heterostructure (and the substrate) highlighted. (b) The self-consistent scheme adopted to study the transport problem: the electrostatic potential $\varphi(z)$ is computed on the left and imposed on the right, where the current through the barrier is computed via the NEGF formalism. From this current, we calculate the time required to trap a small charge ΔQ, so that $Q(z_{\rm FG}; t + \Delta t) = Q(z_{\rm FG}; t) + \Delta Q$. The new charge changes the electrostatic potential in the device and the procedure is repeated until full equilibrium is reached.

current per unit area:

$$I = \frac{2e}{\hbar} \int T(E) \left[f\left(E - \mu_g\right) - f\left(E - \mu_c\right) \right] \mathrm{d}E, \qquad (8)$$

where f is the Fermi-Dirac distribution function.

The entire procedure is implemented in the NanoTCAD ViDES toolkit, which efficiently solves both the electrostatics and the charge-transport problems. In Fig. 7, one can appreciate the leakage currents at different values of V_{gc} for varying barrier widths, showing a clear exponential dependence on the barrier width (each additional monolayer of h-BN reduces the leakage current by more than 2 orders of magnitude) and a subexponential dependence on the applied voltage, as expected.

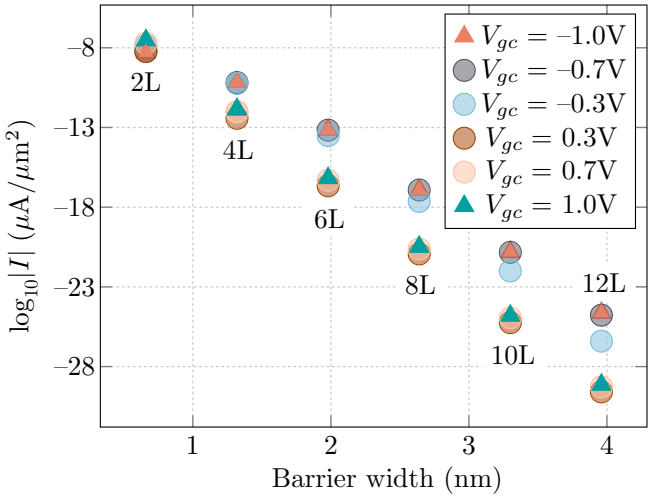

FIG. 7. A comparison of the gate-leakage current versus the barrier width in a FET composed of a monolayer MoS_2 channel, a monolayer Gr gate, and a multilayer h-BN barrier (2L, two layers; ... ; 12L, 12 layers), for various applied gate-channel voltages V_{gc}. A $n = 5 \times 10^{12}$ cm^{-2} doping is imposed on the channel.

B. Floating-gate memory

As depicted in Fig. 6(a), we consider the core heterostructure and put a metallic control gate (CG) and a second insulating h-BN multilayer block between the Gr gate and the substrate; thus making the Gr monolayer a floating gate (FG). Devices like this one have recently attracted a lot of interest in experimental research [10,38–41]. In this case, $\varphi(z_{\rm CG})$ is fixed by imposing Dirichlet boundary conditions, which are appropriate for an ideal metal, while $\varphi(z_{\rm ch})$ is subject to Neumann boundary conditions. Importantly, here the charge $Q(z_{\rm FG})$ trapped in the FG changes over time. Due to our multiscale methodology, we are able to investigate such time dependence with low computational efforts and a quasiatomistic accuracy. The simulation proceeds as follows [see Fig. 6(b)]. At the initial time $t_0 = 0$, a certain charge $Q(z_{\rm ch}; t_0)$ is present in the channel and a charge $Q(z_{\rm FG}; t_0)$ is trapped in the floating gate. If $D_{\rm gr}[E - \varphi(z_{\rm FG}; t_i)]$ is the density of states for graphene when the potential is $\varphi(z_{\rm FG}; t_i)$, then the floating-gate electrochemical potential $\mu_{\rm FG}(t_i)$ is obtained by inverting Eq. (7). Note that the integral has to be taken from the Dirac-cone energy μ_0 to $\mu_{\rm FG}(t_i)$ itself. The tunneling current is computed by applying Eq. (8), with $\mu_{\rm FG}(t)$ in place of μ_g. Taking a small incremental time step Δt in the simulation and assuming a fast energy-relaxation rate in the floating gate, we expect the process to be adiabatic. Then, at $t + \Delta t$, the charge in the floating gate has changed linearly with the tunneling current across the barrier, $I(t)$:

$$Q(z_{\rm FG}, t + \Delta t) = Q(z_{\rm FG}, t) - \Delta t\, I(t). \qquad (9)$$

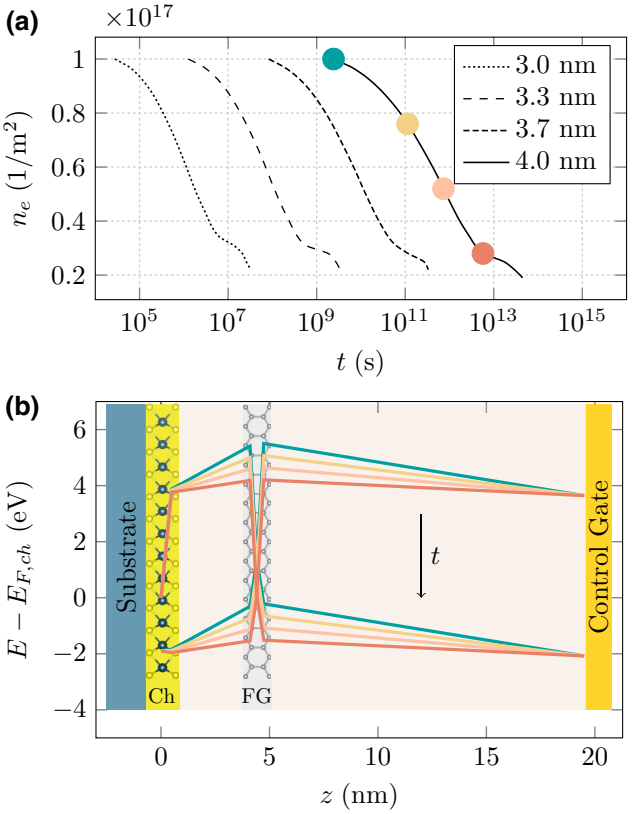

FIG. 8. (a) The time evolution of the charge trapped on the floating gate for different barrier widths, from 10 to 13 *h*-BN layers. In all cases, a 16.3-nm-thick insulator separates the floating and control gates, a $n = 2 \times 10^{13}$ cm^{-2} doping is considered for the MoS_2 channel, and V_{gc} is fixed at 0.0 V. Note that the initial potential on the floating gate depends on the barrier width. The band structure at different times for the 13–*h*-BN–layer evolution curve (the colored dots) is reported in (b), where matching colors refer to the same time *t*.

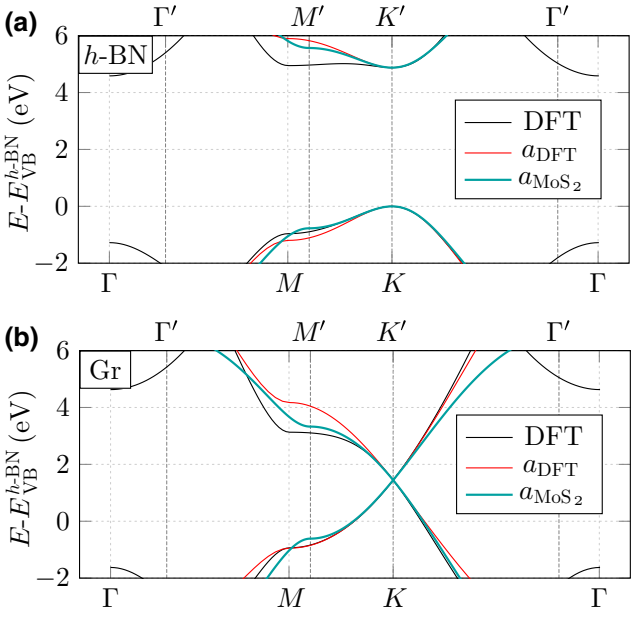

FIG. 9. A comparison of the bands, centered around the *K* point, for Gr and *h*-BN as obtained from DFT, the tight-binding best fit on the same lattice parameter as DFT, and the tight-binding best fit on the common lattice. The high-symmetry points in the bottom axis refer to the first Brillouin zone relative to the DFT lattice ($a_{DFT} = 0.246$ nm for both materials); whereas the primed ones, on the top axis, refer to the first Brillouin zone relative to the common lattice ($a_{VH} = a_{MoS_2}$).

Equations (6)–(9) are solved again after another time step Δt, and so on until saturation. In Fig. 8, we present the retention times of the charges trapped on the floating gate. The exponential dependence over the barrier width is again evident: more than 2 orders of magnitude of retention time are gained with every new layer of *h*-BN.

V. CONCLUSION

We present a computationally effective and physically sound method to simulate electronic transport in 2D van der Waals heterostructures based on a multiscale approach and quasiatomistic Hamiltonians, and we apply it to example use cases of electronic devices based on 2D materials—namely a FET and a floating-gate memory, composed of molybdenum disulphide, hexagonal boron nitride, and graphene.

This method maps the complex Hamiltonian of a large van der Waals heterostructure into an effective pseudoatomistic Hamiltonian with a uniform three-dimensional (3D) lattice geometry, where all the effects due to the presence of different layer geometry, orientation, and interactions are taken into account in the values of the tight-binding parameters, while the structure of the Hamiltonian is fixed.

This approach entails a significant degree of approximation but also enables the simulation of devices based on vertical heterostructures that would be prohibitive with fully atomistic Hamiltonians. At the same time, it provides a physically sounder route than common approximations such as the Tsu-Esaki formula, which in the case of a van der Waals heterostructure of 2D materials would not be able to capture the richness of the material properties and the impact of the variation of the Hamiltonian associated with different layers on charge transport in the transversal direction for a complex device. The input files for the DFT simulations can be found in an online repository at Ref. [61].

ACKNOWLEDGMENTS

This work was partially supported by the European Union Horizon 2020 Framework Programme under the "Quantum Engineering for Machine Learning" (QUEFORMAL) project (Grant Agreement No. 829035) and by

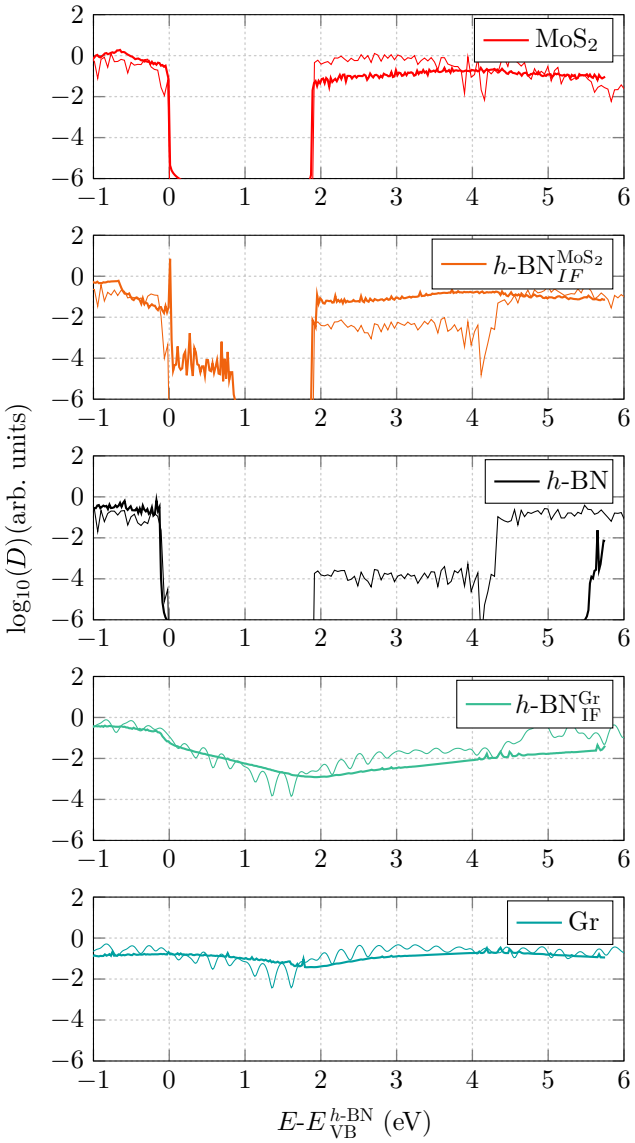

FIG. 10. The DFT (thin) versus the tight-binding (thick) LDOS for the two heterostructures h-BN/MoS_2/h-BN and Gr/h-BN/Gr.

the Italian Ministry of University and Research through the PRIN project FIVE2D (2017SRYEJH 001), the Graphene Flagship Core 3 (Contract No. 881603), and the Crosslab Department of Excellence project.

APPENDIX A: BAND STRUCTURES IN THE COMMON LATTICE

For the DFT simulations, we consider the lattice parameters $a_i = 0.246$ nm for $i =$ (Gr, h-BN) and $a = 0.307$ nm for MoS_2, as reported in the main text. For each material, the fitting procedure for the in-plane tight-binding parameters is standard: we select the parameters that give the best fit for the band structures around the K points. Then, by moving to the common lattice, we resize each first Brillouin zone to that of MoS_2. In Fig. 9 we show a direct comparison of the valence and conduction bands for Gr and h-BN in the three cases: the DFT simulations, the tight-binding best fit with the lattice parameter obtained from DFT ($a = 0.246$ nm), and the tight binding on the common lattice with $a_{\mathrm{VH}} = 0.307$ nm $= a_{\mathrm{MoS_2}}$.

APPENDIX B: DOS COMPARISON: DFT VERSUS TIGHT BINDING

In Fig. 10 we show a detailed comparison of the density of states between two cases:

(a) Thick lines: DOS as computed from NEGF in the tight-binding model of a MoS_2/h-BN/Gr heterostructure, where multiple layers of h-BN are considered. The "h-BN$^X_{IF}$" labels refer to the h-BN layer adjacent to material X.

(b) Thin lines: DOS as computed from DFT in either the h-BN–MoS_2–h-BN system or the Gr–h-BN–Gr one.

APPENDIX C: DETAILS OF THE *h*-BN MODELING

The h-BN band gap is different in the DFT and tight-binding cases. This is due to the fact that vertical transport in this material seems to ignore some states in the conduction band, as can be seen from Fig. 11.

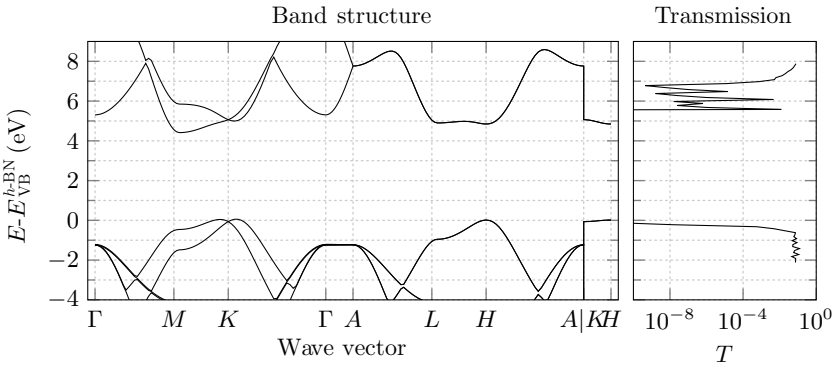

FIG. 11. The DFT results for a 12-layer h-BN structure. As the transmission spectrum presents a wider gap than that predicted by the band structure, the wider value is taken as a reference for the tight-binding modeling of h-BN.

The band structure is computed with the help of QUANTUM ESPRESSO and the transmission spectrum with PWCOND, as explained in the main text.

[1] K. S. Novoselov, A. Mishchenko, A. Carvalho, and A. H. C. Neto, 2D materials and van der Waals heterostructures, Science **353**, aac9439 (2016).

[2] K. Cho, J. Pak, S. Chung, and T. Lee, Recent advances in interface engineering of transition-metal dichalcogenides with organic molecules and polymers, ACS Nano **13**, 9713 (2019).

[3] G. Iannaccone, F. Bonaccorso, L. Colombo, and G. Fiori, Quantum engineering of transistors based on 2D materials heterostructures, Nat. Nanotechnol. **13**, 183 (2018).

[4] F. Capasso, Band-gap engineering: From physics and materials to new semiconductor devices, Science **235**, 172 (1987).

[5] C.-Y. Wang, S.-J. Liang, S. Wang, P. Wang, Z. Li, Z. Wang, A. Gao, C. Pan, C. Liu, J. Liu, *et al.*, Gate-tunable van der Waals heterostructure for reconfigurable neural network vision sensor, Sci. Adv. **6**, eaba6173 (2020).

[6] C. Liu, X. Yan, X. Song, S. Ding, D. W. Zhang, and P. Zhou, A semi-floating gate memory based on van der Waals heterostructures for quasi-non-volatile applications, Nat. Nanotechnol. **13**, 404 (2018).

[7] D. U. Lim, S. Choi, S. Kim, Y. J. Choi, S. Lee, M. S. Kang, Y.-H. Kim, and J. H. Cho, All-inkjet-printed vertical heterostructure for wafer-scale electronics, ACS Nano **13**, 8213 (2019).

[8] T. Wang, Q. Zhang, J. Li, and C. Xia, 2D GeSe/SnS_2($SnSe_2$) broken-gap heterostructures for tunnel field-effect transistors applications, J. Phys. D: Appl. Phys. **52**, 455103 (2019).

[9] L. Britnell, R. V. Gorbachev, R. Jalil, B. D. Belle, F. Schedin, A. Mishchenko, T. Georgiou, M. I. Katsnelson, L. Eaves, S. V. Morozov, N. M. R. Peres, J. Leist, A. K. Geim, K. S. Novoselov, and L. A. Ponomarenko, Field-effect tunneling transistor based on vertical graphene heterostructures, Science **335**, 947 (2012).

[10] Q. A. Vu, Y. S. Shin, Y. R. Kim, V. L. Nguyen, W. T. Kang, H. Kim, D. H. Luong, I. M. Lee, K. Lee, D.-S. Ko, J. Heo, S. Park, Y. H. Lee, and W. J. Yu, Two-terminal floating-gate memory with van der Waals heterostructures for ultrahigh on/off ratio, Nat. Commun. **7**, 12725 (2016).

[11] J. Li, X. Chen, D. W. Zhang, and P. Zhou, Van der Waals heterostructure based field effect transistor application, Crystals **8**, 8 (2018).

[12] F. Liu, W. T. Navaraj, N. Yogeswaran, D. H. Gregory, and R. Dahiya, van der Waals contact engineering of graphene field-effect transistors for large-area flexible electronics, ACS Nano **13**, 3257 (2019).

[13] J. Cheng, C. Wang, X. Zou, and L. Liao, Recent advances in optoelectronic devices based on 2D materials and their heterostructures, Adv. Opt. Mater. **7**, 1800441 (2018).

[14] S. Kang, D. Lee, J. Kim, A. Capasso, H. S. Kang, J.-W. Park, C.-H. Lee, and G.-H. Lee, 2D semiconducting materials for electronic and optoelectronic applications: Potential and challenge, IOP Publishing **7**, 022003 (2020).

[15] S. Bruzzone, D. Logoteta, G. Fiori, and G. Iannaccone, Vertical transport in graphene-hexagonal boron nitride heterostructure devices, Sci. Rep. **5**, 14519 (2015).

[16] Q. Qian, J. Lei, J. Wei, Z. Zhang, G. Tang, K. Zhong, Z. Zheng, and K. J. Chen, 2D materials as semiconducting gate for field-effect transistors with inherent over-voltage protection and boosted on-current, npj 2D Mater. Appl. **3**, 24 (2019).

[17] G. Fiori, S. Bruzzone, and G. Iannaccone, Very large current modulation in vertical heterostructure graphene/hBN transistors, IEEE Trans. Electron Devices **60**, 268 (2013).

[18] S. Bertolazzi, D. Krasnozhon, and A. Kis, Nonvolatile memory cells based on MoS_2/graphene heterostructures, ACS Nano **7**, 3246 (2013).

[19] G. Migliato Marega, Y. Zhao, A. Avsar, Z. Wang, M. Tripathi, A. Radenovic, and A. Kis, Logic-in-memory based on an atomically thin semiconductor, Nature **587**, 72 (2020).

[20] Q. Zhang, G. Fiori, and G. Iannaccone, On transport in vertical graphene heterostructures, IEEE Electron Device Lett. **35**, 966 (2014).

[21] Y. Cao, V. Fatemi, S. Fang, K. Watanabe, T. Taniguchi, E. Kaxiras, and P. Jarillo-Herrero, Unconventional superconductivity in magic-angle graphene superlattices, Nature **556**, 43 (2018).

[22] M. Elstner, D. Porezag, G. Jungnickel, J. Elsner, M. Haugk, T. Frauenheim, S. Suhai, and G. Seifert, Self-consistent-charge density-functional tight-binding method for simulations of complex materials properties, Phys. Rev. B **58**, 7260 (1998).

[23] M. Brandbyge, J.-L. Mozos, P. Ordejón, J. Taylor, and K. Stokbro, Density-functional method for nonequilibrium electron transport, Phys. Rev. B **65**, 165401 (2002).

[24] N. Papior, N. Lorente, T. Frederiksen, A. García, and M. Brandbyge, Improvements on non-equilibrium and transport Green function techniques: The next-generation TRANSIESTA, Comput. Phys. Commun. **212**, 8 (2017).

[25] S. Datta, Nanoscale device modeling: The Green's function method, Superlattices Microstruct. **28**, 253 (2000).

[26] Z. Ren, R. Venugopal, S. Goasguen, S. Datta, and M. S. Lundstrom, nanoMOS 2.5: A two-dimensional simulator for quantum transport in double-gate MOSFETs, IEEE Trans. Electron Devices **50**, 1914 (2003).

[27] R. Tsu and L. Esaki, Tunneling in a finite superlattice, Appl. Phys. Lett. **22**, 562 (1973).

[28] N. C. Kluksdahl, A. M. Kriman, D. K. Ferry, and C. Ringhofer, Self-consistent study of the resonant-tunneling diode, Phys. Rev. B **39**, 7720 (1989).

[29] W. R. Frensley, Boundary conditions for open quantum systems driven far from equilibrium, Rev. Mod. Phys. **62**, 745 (1990).

[30] G. Iannaccone, G. Lombardi, M. Macucci, and B. Pellegrini, Enhanced Shot Noise in Resonant Tunneling: Theory and Experiment, Phys. Rev. Lett. **80**, 1054 (1998).

[31] R. C. Bowen, G. Klimeck, R. K. Lake, W. R. Frensley, and T. Moise, Quantitative simulation of a resonant tunneling diode, J. Appl. Phys. **81**, 3207 (1997).

[32] K. A. Guerrero-Becerra, A. Tomadin, and M. Polini, Resonant tunneling and the quasiparticle lifetime in graphene/boron nitride/graphene heterostructures, Phys. Rev. B **93**, 125417 (2016).

[33] B. Amorim, R. M. Ribeiro, and N. M. R. Peres, Multiple negative differential conductance regions and inelastic phonon assisted tunneling in graphene/$h-$BN/graphene structures, Phys. Rev. B **93**, 235403 (2016).

[34] A. Grüneis, C. Attaccalite, L. Wirtz, H. Shiozawa, R. Saito, T. Pichler, and A. Rubio, Tight-binding description of the quasiparticle dispersion of graphite and few-layer graphene, Phys. Rev. B **78**, 205425 (2008).

[35] S. Reich, J. Maultzsch, C. Thomsen, and P. Ordejón, Tight-binding description of graphene, Phys. Rev. B **66**, 035412 (2002).

[36] M. Yankowitz, Q. Ma, P. Jarillo-Herrero, and B. J. LeRoy, van der Waals heterostructures combining graphene and hexagonal boron nitride, Nat. Rev. Phys. **1**, 112 (2019).

[37] X. Yu, G. Zhao, C. Liu, C. Wu, H. Huang, J. He, and N. Zhang, A MoS_2 and graphene alternately stacking van der Waals heterostructure for Li^+/Mg^{2+} co-intercalation, Adv. Funct. Mater. **n/a**, 2103214.

[38] Y.-H. Zhang and T. Senthil, Bridging Hubbard model physics and quantum Hall physics in trilayer graphene/h-BN moiré superlattice, Phys. Rev. B **99**, 205150 (2019).

[39] M. A. Rodder, S. Vasishta, and A. Dodabalapur, Double-gate MoS_2 field-effect transistor with a multilayer graphene floating gate: A versatile device for logic, memory, and synaptic applications, ACS Appl. Mater. Interfaces **12**, 33926 (2020).

[40] D. Li, X. Wang, Q. Zhang, L. Zou, X. Xu, and Z. Zhang, Nonvolatile floating-gate memories based on stacked black phosphorus–boron nitride–MoS_2 heterostructures, Adv. Funct. Mater. **25**, 7360 (2015).

[41] J. Wang, X. Zou, X. Xiao, L. Xu, C. Wang, C. Jiang, J. C. Ho, T. Wang, J. Li, and L. Liao, Floating gate memory-based monolayer MoS_2 transistor with metal nanocrystals embedded in the gate dielectrics, Small **11**, 208 (2015).

[42] R. Schlaf, O. Lang, C. Pettenkofer, and W. Jaegermann, Band lineup of layered semiconductor heterointerfaces prepared by van der Waals epitaxy: Charge transfer correction term for the electron affinity rule, J. Appl. Phys. **85**, 2732 (1999).

[43] S. L. Howell, D. Jariwala, C.-C. Wu, K.-S. Chen, V. K. Sangwan, J. Kang, T. J. Marks, M. C. Hersam, and L. J. Lauhon, Investigation of band-offsets at monolayer-multilayer MoS_2 junctions by scanning photocurrent microscopy, Nano Lett. **15**, 2278 (2015).

[44] J. DiStefano, Y.-C. Lin, J. Robinson, N. R. Glavin, A. A. Voevodin, J. Brockman, M. Kuhn, B. French, and S. W. King, Band alignment at molybdenum disulphide/boron nitride/aluminum oxide interfaces, J. Electron. Mater. **45**, 983 (2016).

[45] Y.-J. Yu, Y. Zhao, S. Ryu, L. E. Brus, K. S. Kim, and P. Kim, Tuning the graphene work function by electric field effect, Nano Lett. **9**, 3430 (2009).

[46] D. Wickramaratne, L. Weston, and C. G. Van de Walle, Monolayer to bulk properties of hexagonal boron nitride, J. Phys. Chem. C **122**, 25524 (2018).

[47] P. Giannozzi, S. Baroni, N. Bonini, M. Calandra, R. Car, C. Cavazzoni, D. Ceresoli, G. L. Chiarotti, M. Cococcioni, I. Dabo, *et al.*, QUANTUM ESPRESSO: A modular and open-source software project for quantum simulations of materials, J. Phys.: Condens. Matter **21**, 395502 (2009).

[48] P. Giannozzi, O. Andreussi, T. Brumme, O. Bunau, M. Buongiorno Nardelli, M. Calandra, R. Car, C. Cavazzoni, D. Ceresoli, M. Cococcioni, *et al.*, Advanced capabilities for materials modelling with QUANTUM ESPRESSO, J. Phys.: Condens. Matter **29**, 465901 (2017).

[49] J. P. Perdew, K. Burke, and M. Ernzerhof, Generalized Gradient Approximation Made Simple, Phys. Rev. Lett. **77**, 3865 (1996).

[50] S. Grimme, Accurate description of van der Waals complexes by density functional theory including empirical corrections, J. Comput. Chem. **25**, 1463 (2004).

[51] O. Hod, Interlayer commensurability and superlubricity in rigid layered materials, Phys. Rev. B **86**, 075444 (2012).

[52] R. J. Hunt, B. Monserrat, V. Zólyomi, and N. D. Drummond, Diffusion quantum Monte Carlo and *gw* study of the electronic properties of monolayer and bulk hexagonal boron nitride, Phys. Rev. B **101**, 205115 (2020).

[53] W. S. Yun, S. W. Han, S. C. Hong, I. G. Kim, and J. D. Lee, Thickness and strain effects on electronic structures of transition metal dichalcogenides: 2H-MX_2 semiconductors ($M =$ Mo, W; $X =$ S, Se, Te), Phys. Rev. B **85**, 033305 (2012).

[54] A. Smogunov, A. Dal Corso, and E. Tosatti, Ballistic conductance of magnetic Co and Ni nanowires with ultrasoft pseudopotentials, Phys. Rev. B **70**, 045417 (2004).

[55] NanoTCAD ViDES, Code and documentation, http://vides.nanotcad.com, accessed: September, 2020.

[56] J. Heyd and G. E. Scuseria, Hybrid functionals based on a screened Coulomb potential, J. Chem. Phys. **118**, 8207 (2003).

[57] L. Hedin, New method for calculating the one-particle Green's function with application to the electron-gas problem, Phys. Rev. **139**, A796 (1965).

[58] S. Latini, K. T. Winther, T. Olsen, and K. S. Thygesen, Interlayer excitons and band alignment in MoS_2/hBN/WSe_2 van der Waals heterostructures, Nano Lett. **17**, 938 (2017).

[59] V. O. Özçelik, J. G. Azadani, C. Yang, S. J. Koester, and T. Low, Band alignment of two-dimensional semiconductors for designing heterostructures with momentum space matching, Phys. Rev. B **94**, 035125 (2016).

[60] A. Laturia, M. L. Van de Put, and W. G. Vandenberghe, Dielectric properties of hexagonal boron nitride and transition metal dichalcogenides: From monolayer to bulk, npj 2D Mater. Appl. **2**, 6 (2018).

[61] G. Calogero, Input SCF data for our simulations in QUANTUM ESPRESSO (2022), https://doi.org/10.5281/zenodo.6623936.